*Int. J. Electrochem. Sci.*, 13 **(2018)** 10654 – 10668, doi: 10.20964/2018.11.25

**International Journal of ELECTROCHEMICAL SCIENCE**
www.electrochemsci.org

# Microstructure and Surface Morphology of Inconel 625 Alloy Prepared by Laser Melting Deposition using Abrasive-Assisted Jet Electrochemical Machining

*Junzhi Liu*[1], *Changshui Gao*[1], *Lida Shen*[1*], *Haixia Cheng*[1], *Xuesong Gao*[2], *and Xiao Han*[3]

[1] College of Mechanical and Electrical Engineering, Nanjing University of Aeronautics and Astronautics, Nanjing 210016, People's Republic of China
[2] Nanjing Institution of Advanced Laser Technology, Nanjing 210038, People's Republic of China
[3] Beijing Institute of Space Mechanics and Electricity, Beijing 100094, People's Republic of China
[*]E-mail: ldshen@nuaa.edu.cn

*Received:* 6 July 2018 / *Accepted:* 19 August 2018 / *Published:* 1 October 2018

Laser melting deposition (LMD) is typically used for forming and repairing large-scale complex nickel-based superalloy parts, such as aero engines. Defects occur on the surface and structure during LMD and after the completion of forming, so LMD-jet electrochemical machining (JECM) hybrid fabrication was proposed, and a novel abrasive-assisted JECM device was designed. The processing time, and the various processing conditions of the hybrid fabrication were investigated, on account of the balance of processing efficiency and quality. Experiments showed that the oxidation layer of the LMDed samples could be removed entirely under the processing of 90 JECM cycles, while the abrasive-assisted soft brush could efficiently remove the electrolytic products and the abrasive-assisted hard grinding head could efficiently remove the hard-to-electrolyze residual particles in the overlapping areas. The organization microstructure and the surface morphology were characterized using a scanning electron microscope and a 3D optical profiler. The influence that a non-homogeneous distribution of grains (both size and orientation) had on JECM was discussed. The fluctuations of the current efficiencies throughout the processes were analyzed and discussed.

**Keywords:** Laser melting deposition; Electrochemical machining; superalloy; Hybrid fabrication; Microstructure; Surface morphology

## 1. INTRODUCTION

Nickel-based superalloys are used to manufacture aero-engine blades, rocket engine parts, and high-temperature components of petrochemical equipment and nuclear reactor equipment, due to their high high-temperature strength and resistance to oxidative corrosion [1-4]. Inconel 718 alloy has

excellent welding performance, high tensile strength, high fatigue strength, high creep resistance and fracture resistance, and high oxidation resistance to high temperatures, while having stable chemical properties at low temperatures. Inconel 625 alloy has the same excellent performance as Inconel 718, but a higher mass fraction of chromium and molybdenum than Inconel 718 alloy, so its corrosion resistance is higher [5]. The laser melting deposition (LMD) is commonly used to deposit nickel-based superalloy large-scale complex components, due to its large fabrication size and high material utilization [6-10]. The industrial robot moves the cladding head according to the tracks generated by the CAE software and the preset process parameters during the LMD shaping process. The cladding head injects metallic powder into a melt-pool created by the laser beam with a specific power density on the substrate. There is usually an oxidation on the surface of the LMDed parts. Therefore, subsequent processing is required. There has been a hybrid fabrication that combines LMD and mechanical machining, but the traditional forming process has more difficulty to machining the nickel-based superalloy parts. Jet electrochemical machining (JECM) is suitable for the subsequent processing of nickel-based superalloy parts, as it has no-tool loss, regardless of the material hardness, high productivity, excellent surface quality, and ability to process complex three-dimensional shapes [11-13].

In this paper, Inconel 625 alloy powder was used to form the LMDed parts. To post-process the LMDed parts, an LMD-JECM hybrid fabrication was proposed, and an abrasive-assisted, flexible, easy-to-transplant JECM device was designed. During the LMD shaping process, the substrate was placed directly on the workbench and required no clamping, so that the JECM device could perform the subsequent processing without any movement and secondary clamping of the forming sample. The abrasive-assisted soft brush composed of biological bristle was used to remove electrolytic viscous products, to facilitate the discharge of electrolytes, and to improve the heat dissipation efficiency of the processing interface. The abrasive-assisted hard grinding head composed of a red corundum grinding wheel was used to remove the hard-to-electrolyze residual particles in the strip-like regions. The purpose of the hybrid fabrication was to reduce the material removal as much as possible, while ensuring a good surface quality of the JECM, so that the surface quality could be improved while ensuring the processing efficiency. The microstructure and surface morphology of the JECMed samples under different processing time and different processing conditions were studied in this paper. There are many researches on ECM of nickel-based superalloy. The paper mainly explores the process of oxidation removal. The causes for the formation of the hard-to-electrolyze residual particles in the strip-like regions were discussed. The feasibility of the hybrid fabrication system and the JECM device were verified.

## 2. EXPERIMENTAL

### *2.1 Experimental system.*

The LMD system performed shaping forming of the metal powder on the substrate placed on the workbench. Following the formation, the LMD system suspended, and the cladding head returned

to the home position. The JECM device was then moved to the surface of the LMDed sample, to perform the electrolytic treatment. If necessary, the LMD system could continue to deposit on the JECMed surface. Fig. 1 depicts the principle of the LMD-JECM hybrid fabrication.

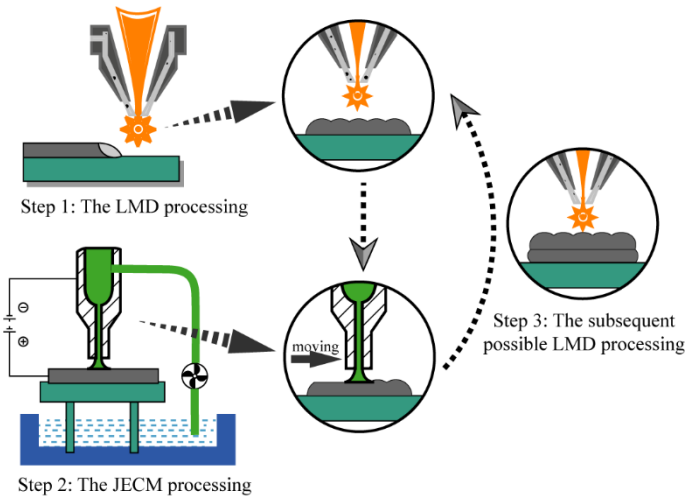


**Figure 1.** Principle of the LMD-JECM hybrid fabrication

The LMD system used in this paper was a High-Power Composite Laser Machining Workstation (Fig. 2a). The entire LMD system consisted of a laser (TruDisk 12003, TRUMPF), a chiller (MCW1-25DTR), an argon cylinder, a cladding head (Siemens), an industrial robot (KUKA), a powder feeding device (GTV PF 2/2) composition, and a computer control system.

The cladding head of the LMD system was controlled by the industrial robot and the shielding gas was ejected from the cladding head. As a result, the workpiece did not require placement in an enclosed environment. The characteristics of the LMD system and the convenience of the switching of hybrid fabrication were taking into account to design an abrasive-assisted JECM device that was compact, flexible, and easy to transplant. The abrasive-assisted JECM device consisted of a JECM cathode, an abrasive-assisted soft brush, an abrasive-assisted hard grinding head, fixing screws, bearings, driving motors, pulleys, belts, and couplings (Fig. 3a). The experimental results revealed that the electrolytic products of oxidation layer continued to adhere to the surface when the LMDed sample was machined by JECM alone. This seriously affected the subsequent electrolytic reaction. For this reason, an abrasive-assisted soft brush composed of biological bristles was added around the JECM cathode, which improved the removal efficiency of the electrolytic products, facilitated the discharge of the electrolytes and improved the heat dissipation efficiency of the processing interface. An abrasive-assisted hard grinding head, composed of a red corundum grinding wheel, was added in order to remove the hard-to-electrolyze residual particles in the strip-like regions. Fig. 3b is a schematic diagram of the processing principle of JECM. Fig. 3c is an actual object picture of the JECM device.

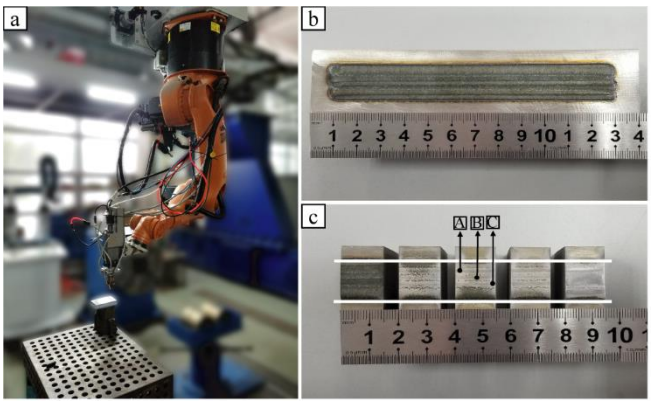


**Figure 2.** The experimental system and experimental samples: (a) the LMD system, (b) LMDed samples, (c) JECMed samples

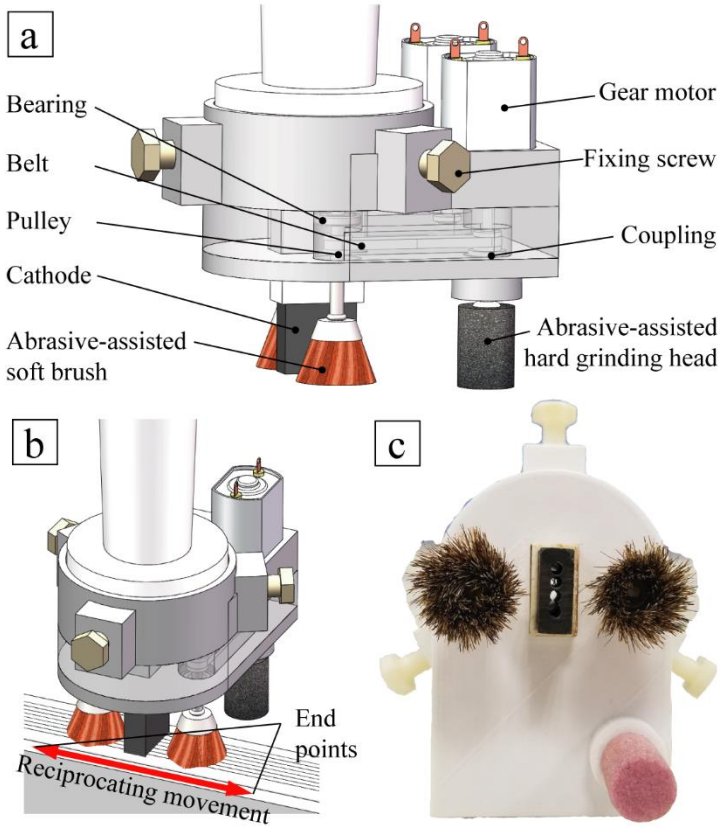


**Figure 3.** Experimental device of JECM. (a) schematic diagram, (b) processing principle, (c) actual object

*2.2 Preparation of samples.*

The multiple beads single-layer samples (Fig. 2b) were fabricated by the LMD system using the Inconel 625 alloy powder. The substrate material was 306L stainless steel and the substrate size was 140mm*30mm*30mm. The processing parameters are listed in Table I. To study the effect of JECM of different processing parameters on the LMDed samples, the LMDed samples were cut into

several 30mm*15mm*30mm subsamples (Fig. 2c) using wire EDM. This ensured that the organization microstructure was the same between subsamples.

The process of the JECM was the reciprocating electrolysis movement of the JECM device controlled by the industrial robot (Fig. 3b). The speed of the reciprocating movement was 10 mm/s and the distance between the end points of the reciprocating movement of the JECM device was 45 mm. The processing time of the JECM was defined by the number of cycles of the reciprocating movement. The total traveling distance was 90mm in one JECM cycle. The width (5mm) of the cathode and the width (15mm) of the sample were taken into account to determine that the actual processing time of the JECM device was 5 seconds, while the working time of the abrasive-assisted soft brush was more than 4 seconds in one JECM cycle. The width of the cladding layer of the LMDed Inconel 625 sample was 15mm. The horizontal width of the designed cathode was also 15mm (in Fig. 2c, the white parallel line is the area swept by the cathode during processing). The processing parameters of the JECM are listed in Table II. Three different processing time (JECM cycles) were studied.

**Table 1.** Processing parameters of LMD

| Processing parameters | Value |
|---|---|
| Laser power(W) | 2800 |
| Scanning rate(mm/min) | 900 |
| Powder feeding rate(g/min) | 6 |
| Overlapping ratio | 50% |

**Table 2.** Processing parameters of JECM

| Processing parameters | Value |
|---|---|
| Voltage(V) | 45 |
| Speed of the reciprocating movement (mm/s) | 10 |
| Initial frontal gap(mm) | 0.5 |
| Electrolyte | 15 wt% NaCl solution |
| Electrolyte flow rate(ml/min) | 130 |
| Electrolyte temperature(℃) | 35 |

**Table 3.** instruments and parameters

| Characterizations | Instruments | Parameters |
|---|---|---|
| Organization structure | SEM(S-3400N) | / |
| Elemental analysis | EDS(S-3400N) | / |
| Surface roughness | Surface Roughness Tester (SRT-6200, LANDTEK) | Number of times 3 |
| Surface morphology | 3D profiler (S-neox, Sensofar) | 0.8mm*0.6mm |

*2.3 Characterization of microstructures and surface morphology.*

To investigate the effect that the different processing time and processing conditions had, the characterizations of the microstructure and surface morphology were characterized via the testing instruments in Table III.

*2.4 Current efficiency measurements.*

The current efficiencies of 30 JECM cycles, 60 JECM cycles, and 90 JECM cycles of the LMDed Inconel 625 sample were measured in order. The current efficiency formula used to characterize the current utilization rate was:

$$\eta = \frac{M}{KIt} * 100\% \quad (1)$$

where K is the electrochemical equivalent (g/(A•h)), I is the processing current (A), and t is the processing time (h). The formula of the electrochemical equivalent of the alloy was:

$$K_{X_1-X_2-\cdots-X_n} = \frac{1}{\frac{X_1\%}{K_{X_1}}+\frac{X_2\%}{K_{X_2}}+\cdots+\frac{X_n\%}{K_{X_n}}} \quad (2)$$

Where $K_{X_1-X_2-\cdots-X_n}$, $K_{X_1}$, $K_{X_2}$, and $K_{X_n}$ are the electrochemical equivalents of Alloy $X_1$-$X_2$- ... -$X_n$ and its constituent elements $X_1$, $X_2$, ... , $X_n$, and $X_1$%, $X_2$%, ... , $X_n$% are the mass percentages of the constituent elements $X_1$, $X_2$, ... , $X_n$.

The working time of the JECM accounts for 55.56% of the entire cycle. The process of JECM used a DC regulated power supply and the processing current changed periodically with the reciprocating movement of the JECM device. The value of I•t was calculated by the integral of recorded curve of the processing current with time. The weight loss of the sample was recorded for 30 JECM cycles, 60 JECM cycles and 90 JECM cycles. The current efficiency was calculated using Eq. (1).

## 3. RESULTS AND DISCUSSION

*3.1 Microstructure.*

Fig. 4 shows the JECMed surface after 90 cycles. The SEM image showed that the surface areas of the JECMed samples were flat regions (Fig. 4c) alternated with strip-like regions (Fig. 4b) covered with hard-to-electrolyze residual particles. Comparing the JECMed Inconel 625 samples (Fig. 2c), it could be seen that the centerline of the strip-like regions and the centerline of the LMDed overlapping areas coincided with each other, while the flat regions coincided with the area between the two adjacent overlapping areas. The experimental result was closely related to the organization microstructure of the LMDed Inconel 625 samples. It then became necessary to analyze solidification process and the organization microstructure.

The LMD shaping process of the Inconel 625 is was performed in three main stages. The melted superalloy powder that absorbed the majority of laser energy, mixed with the micro-melted substrate or the last deposited meal that consumed the remaining laser energy, formed the melt-pool. The convection mechanism of the metal inside the melt-pool (the second stage) then began (Fig. 5a). The convection was caused by the interactions within the temperature gradient resulting from the high laser heating rate, the surface tension difference, and the gravity in the melt-pool. There are thought to be two convection mechanisms in the melt-pool, primarily the central double-ring convection A, where the bottom of the pool circulates to the top, and the convection B, on both sides of the melt-pool [14,15]. Convection A drove the distribution of the alloying elements to be as even as possible and also made the melt-pool spread along the surface of the substrate [16,17]. Convection B was at the edge of the melt-pool, which ensured the shape of the melt-pool and caused the merging of the substrate materials, which diluted the melted alloy elements [18,19]. The third stage was the rapid solidification of the melted metal in the melt-pool. The liquid-solid interface gradually moved to the inside of the melt-pool. The heat accumulation caused the temperature gradient to decrease and then the cell cellular grains formed. Dendrites appeared with the formation of cellular grains [20]. In the upper section of the cladding layer, the temperature gradient along the laser scanning direction was relatively large. Dendrites easily formed parallel to the laser scanning direction [21]. Yuan Chen et al. [22] found that when the laser is perpendicular to the substrate surface, the heat dissipating direction in the substrate is divided into vertically downward components and two lateral components horizontal to the laser scanning direction, while the total heat dissipating direction vector points to the lower left. This is indicated by the dashed arrow in Fig. 5b. The solidification theory shows that the direction of the columnar dendrites growth in the bottom of the cladding layer was inclined to the vertical plane of the laser scanning direction and was biased toward the direction of the laser scanning.

The single bead deposition process of Inconel 625 could thoroughly explain the organization microstructure of the flat regions in Fig. 4c. The strip-like regions were covered with the hard-to-electrolyze residual particles, due to the multiple beads deposition effect. Fig. 6c shows that there were some residual micro-melted alloy powders on the deposition surface [23]. Aggregation of the micro-melted particles also existed in both the melt-pool sides meeting with the substrate. When a bead of deposition completed and the next adjacent bead was deposited, the overlapping region was reheated and melted. The residual micro-melted powder and the newly-created micro-melted powder could be embedded in the overlapping area of the melt-pool. The reheating influence caused the grain orientation of the overlapping region to change and dendrites continued to grow, which formed coarser grains. The analysis of energy dispersive spectrometer (EDS) in the regions seen in Fig. 4b showed that the residual particles had a higher carbon and oxygen content. Therefore, it could be inferred that the strip-like regions were composed of the coarse grains with reheat growth and orientation changes, as well as the surface-oxidized micro-melted alloy powders [24]. Residual particles were not easily electrolyzed, due to the high carbon and oxygen content of the surface. These residual structures typically remained until other processes became involved or prolonging processing time. Fig. 6a is the overlapping region of the LMDed Inconel 625 sample. Fig. 6b is the region between two overlapping regions. The comparison of the surface region showed that the organization microstructure of the overlapping region is more homogeneous, due to the reheating effect.

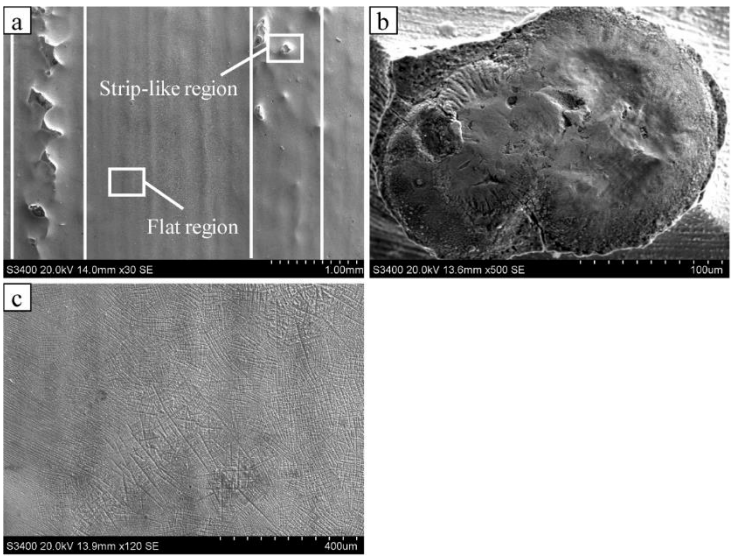


**Figure 4.** SEM images of sample surface machined by 90 JECM cycles. High-magnification images of (b) the strip-like region and (c) the flat region.

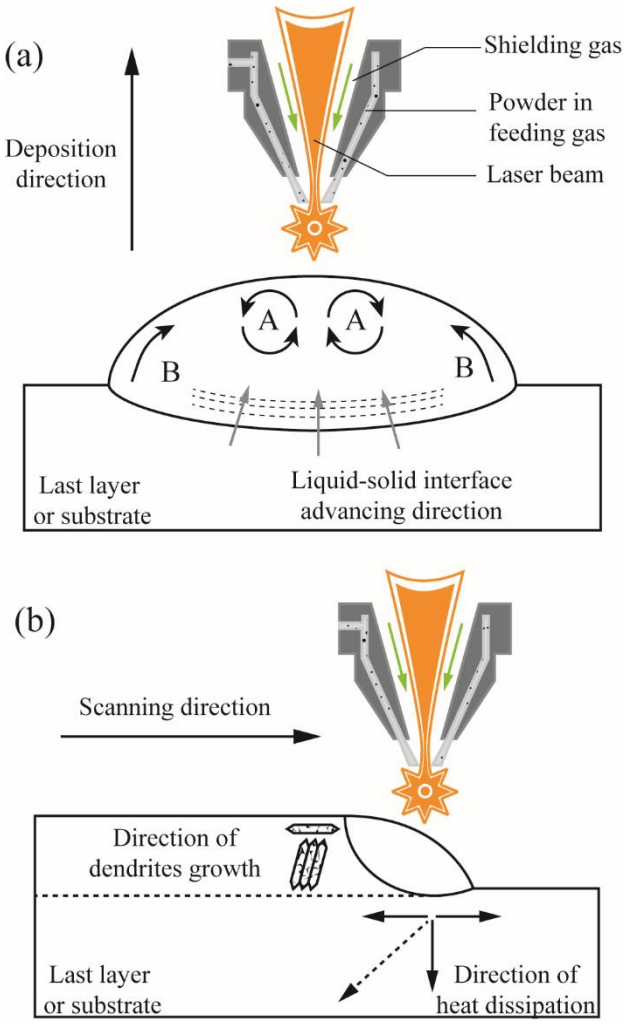


**Figure 5.** Solidification process of melt-pool in laser melting deposition. (a) convection mechanism, (b) dendrites growth and heat dissipation.

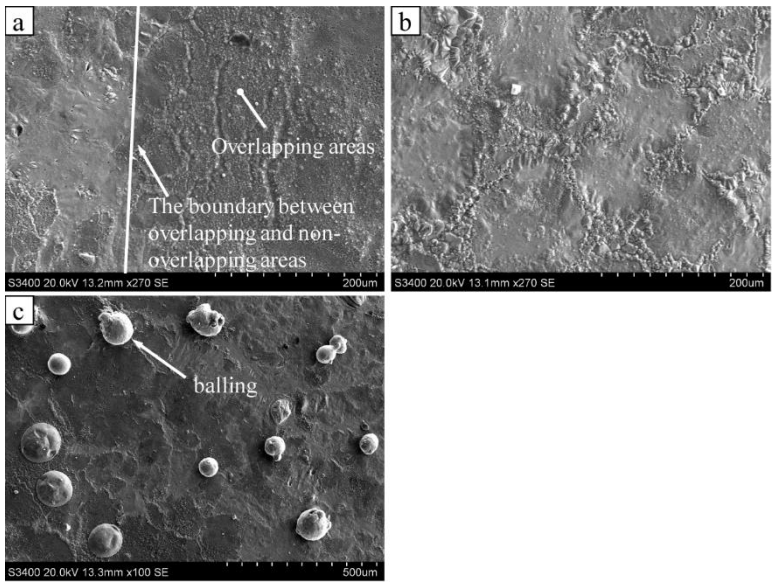


**Figure 6.** SEM images of oxide layer. (a) border between overlapping and non-overlapping areas, (b) non-overlapping areas, (c) balling in the oxide layer.

*3.2 Surface morphology.*

The effects that different processing time and different processing conditions of the JECM had on the surface morphology of the LMDed samples are discussed. When the LMDed Inconel 625 samples were directly processed by JECM in the initial experiment, the result showed that the electrolyzed oxidation layer stuck to the sample surface in a sheet-like structure. There was no mechanical force other than the flow of the electrolyte between the cathode and the sample, so these electrolytic products remained on the sample surface, even though they would be easily removed under the external force. The abrasive-assisted soft brush was added to remove the electrolytic viscous products, to facilitate the discharge of the electrolyte, and to improve the heat dissipation efficiency of the processing interface [25]. An abrasive-assisted hard grinding head was provided to eliminate the strip-like regions covered with residual particles. Fig. 7 depicts the entire process. In Fig. 7a, the JECM cathode and the abrasive-assisted soft brush worked together to remove the oxidation layer and the partial alloy of the LMDed Inconel 625 sample. In Fig. 7b, the abrasive-assisted hard grinding head acted alone to remove the hard-to-electrolyze residual particles in the strip-like regions and to further flatten the entire processed surface. The ECM was a highly efficient and precise machining method. Although the machining accuracy was slightly lower than the grinding accuracy, the machining efficiency was much higher than the grinding efficiency. As a result, there was only one grinding cycle after 90 JECM cycles to remove the hard-to-electrolyze residual particles.

Fig. 8 depicts the change in the surface topography of two regions of the same piece at different processing time. Fig. 8a1, 8a2, and 8a3 depict the surface topography of the flat region in Fig. 4c after 30 cycles, 60 cycles, and 90 cycles. Fig. 8b1, 8b2, and 8b3 depict the surface topography of the stripe-like regions in Fig. 4b after 30 cycles, 60 cycles, and 90 cycles. Fig. 9 is a cross-sectional SEM image perpendicular to laser scanning direction of the LMDed Inconel 625 sample. The image shows that the

average thickness of the surface oxidation layer of the LMDed Inconel 625 sample was about 30um and there were pits and micro-melted particles about 100um in diameter [26]. This also explained the surface topography of 30 JECM cycles (Fig. 8a1). There was a lack of processing time, so the oxidation layer of the sample could not be completely dissolved. And the surface oxidation layer was not a homogeneous structure. The existence of some residual particles and pits led to inhomogeneity of the electrolytic reaction. Therefore, the microscopic surface had some ridge-like protrusion areas. As processing time increased (Fig. 8a2), the microscopic surface area is more even, although some little particles remained. By 90 cycles (Fig. 8a3), the microscopic surface had no defects, was smooth, and the distribution of dendrites were clearly seen. Notably, the dissolution rates of dendrites and inter-dendritic areas were different [27]. The changes of surface morphology with the processing time of the strip-like regions in Fig. 8b series were roughly consistent with the flat regions in Fig. 8a series. It can be seen that hard-to-electrolyze residual particles existed from the outset and some ridge-like regions were extended around them as the center (Fig. 8b1). As the processing time increased, the ridge-like region that extended to the periphery gradually disappeared and eventually the isolated irregular bulge particles were left.

In order to remove the residual particles in strip-like regions after 90 JECM cycles, one cycle of the abrasive-assisted hard grinding head was applied. Although continuing to increase the time of JECM would remove the residual particles in the strip-like regions and make the entire surface have a higher surface quality, this would also lead to the removal of excess material and ultimately affect the efficiency of the entire hybrid fabrication. Our goal was to reduce the removal of the material as much as possible, while ensuring the quality of JECM in order to improve the processing efficiency. Fig. 10 depicts the microscopic surface topography of the sample after 90 JECM cycles and one grinding cycle. Fig. 10b shows a high magnification image of the strip-like region. The hard-to-electrolyze residual particles were easily removed and the grinding surface was smooth. The hard grinding head also further flattened the flat region (Fig. 10c) and the 3D profile comparison (Fig. 12) of the unprocessed LMDed sample and the sample machined by 90 JECM cycles showed that the surface of the processed sample was more even.

Fig. 2c defines the three areas as A, B, and C. The surface roughness of the unprocessed and the different processing time and processing conditions in these three areas were measured (Fig. 11). The surface roughness values of areas A, B, and C gradually reduced from the unprocessed to 30 JECM cycles, 60 JECM cycles, 90 JEDM cycles, and 90 JECM cycles with an additional grinding cycle. The value of the surface roughness after 30 JECM cycles in area A and B was higher than the unprocessed sample because of the incomplete and non-homogeneous electrolytic reaction.

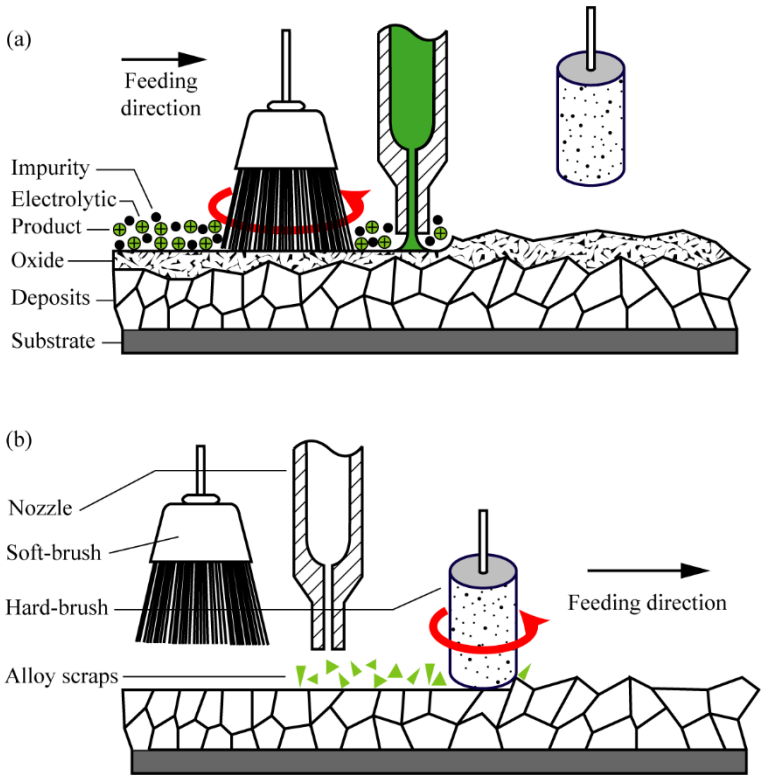


**Figure 7.** Principle of the abrasive-assisted jet electrochemical machining. (a) process of the JECM cycle, (b) process of the grinding cycle.

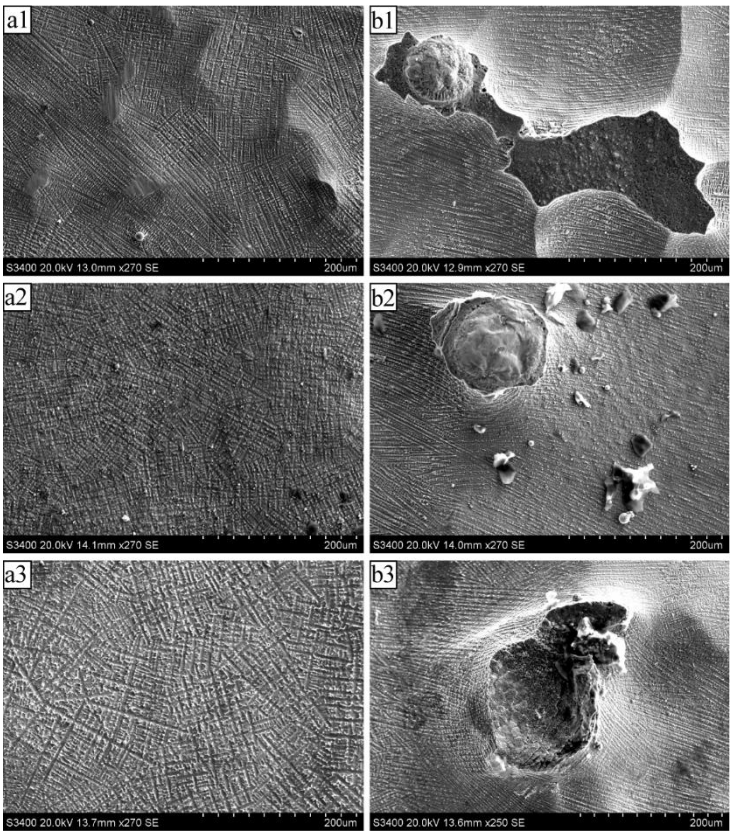


**Figure 8.** SEM images of (a1)-(a3) the flat regions and (b1)-(b3) the strip-like regions machined by 30 JECM cycles, 60 JECM cycles, and 90 JECM cycles respectively.

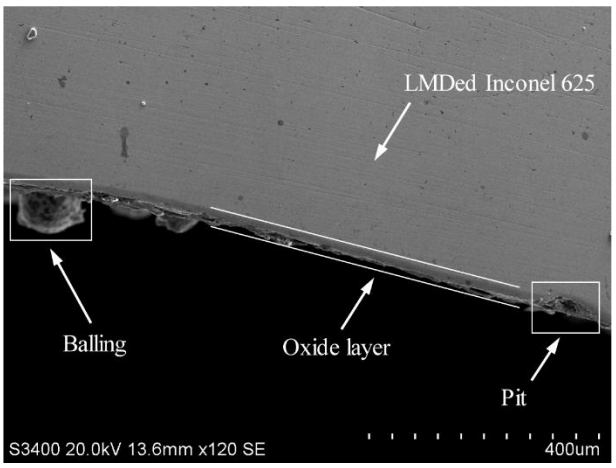


**Figure 9.** SEM image of oxide layer cross section

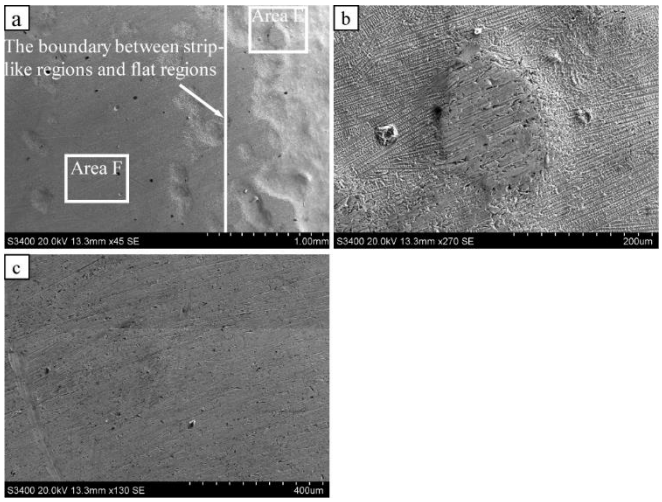


**Figure 10.** SEM images of sample surface machined by 90 JECM cycles with an additional grinding cycle. High-magnification images of (b) the strip-like regions in area E and (c) the flat regions in area F.

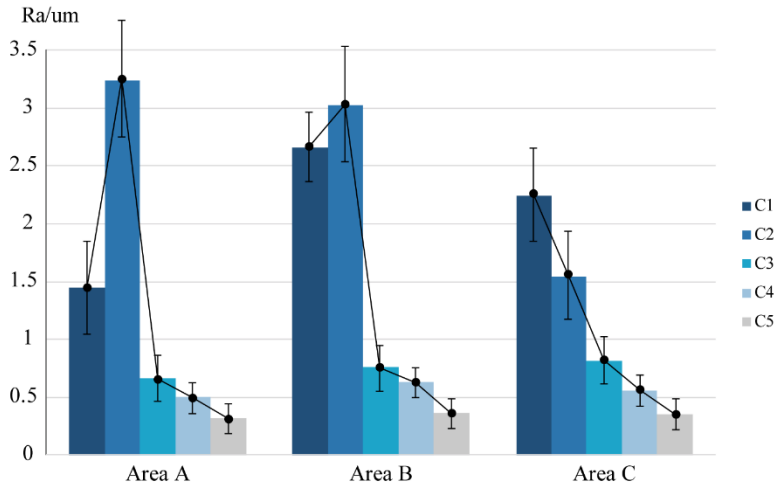


**Figure 11**. Surface roughness of Area A, Area B, and Area C under different processing conditions. C1: LMDed samples, C2: 30 JECM cycles, C3: 60 JECM cycles, C4: 90JECM cycles, and C5: 90 JECM cycles with an additional grinding cycle.

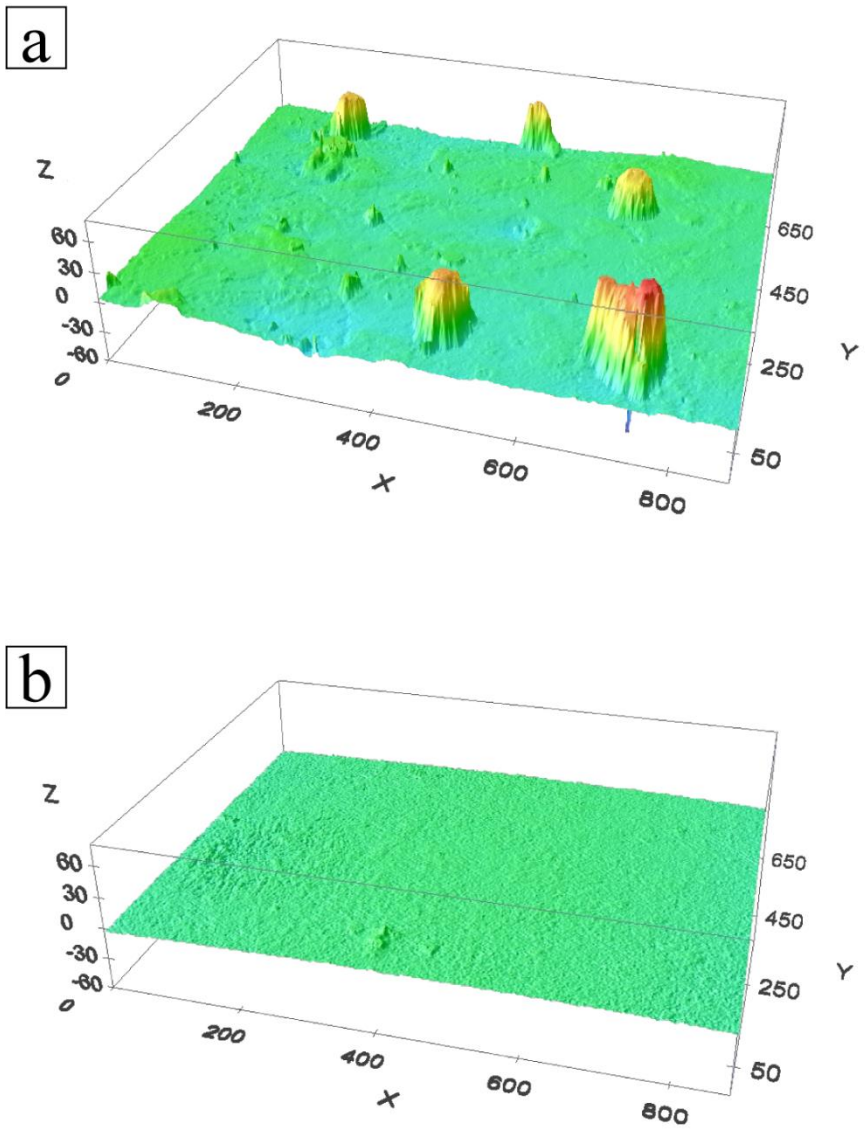


**Figure 12.** 3D profile of (a) the LMDed sample surface and (b) the sample surface machined by 90 JECM cycles.

*3.3 Current efficiency.*

The current efficiencies of 0-30 JECM cycles, 0-60 JECM cycles, 0-90 JECM cycles, 30-60 JECM cycles and 60-90 JECM cycles were measured (Fig. 13). The current efficiency of 0-30 JECM cycles exceeded 100%, because the oxidation layer was removed by electrolysis. And it was not a uniform removal of a single iron one by one, but the oxidation layer piece by piece.[12] The current efficiency of 60-90 JECM cycles principally reflected the current efficiency of the Inconel 625 alloy sample without an oxidation layer.

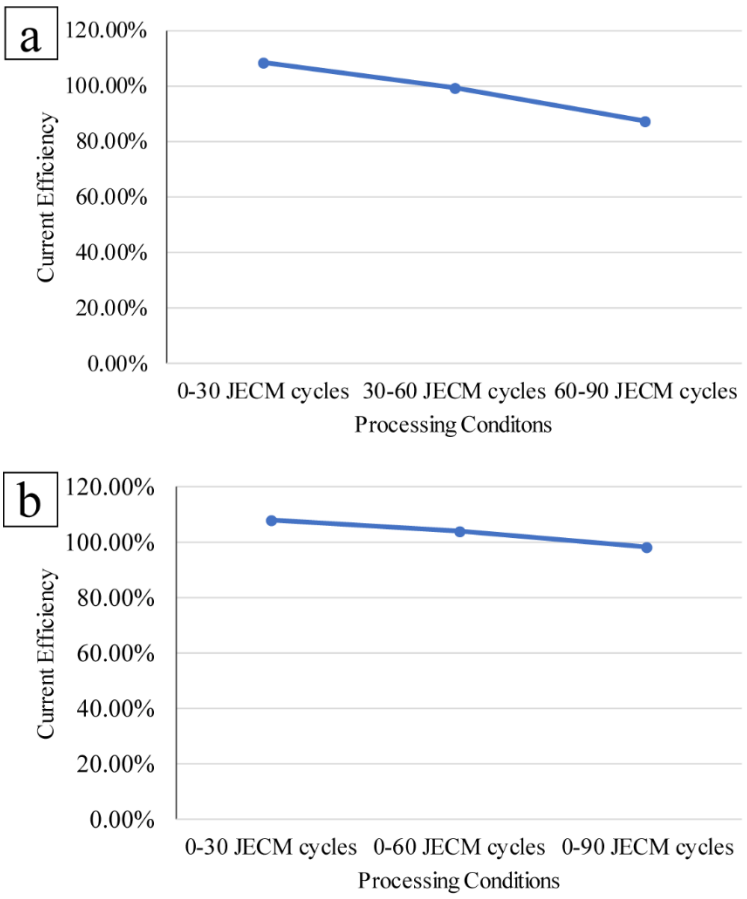


**Figure 13.** Current efficiency curves. (a) 0-30 JECM cycles, 0-60 JECM cycles, and 0-90 JECM cycles; (b) 0-30 JECM cycles, 30-60 JECM cycles and 60-90 JECM cycles.

## 4. CONCLUSIONS

(1) The abrasive-assisted JECM device designed in this paper was compact, flexible and easy-to-transplant. While the LMD system used an industrial robot to move the cladding head in a semi-enclosed environment and the substrate does not require clamping, the abrasive-assisted JECM device could be easily installed on the industrial robot to become a subsequent process, as well as an in-situ hybrid fabrication.

(2) The experiment proved that the abrasive-assisted soft brush head efficiently removed the electrolytic products, facilitated the discharge of electrolytes, and improved the heat dissipation efficiency of the processing interface, while the abrasive-assisted hard grinding head efficiently removed the hard-to-electrolyze residual particles in the strip-like regions.

(3) JECM is as a non-contact, non-forced, untraditional processing method, that could be used to study the organization microstructure in the designated area of the LMDed sample.

(4) The LMD-JECM hybrid fabrication compensated for the shortage of the LMD-traditional mechanical machining hybrid fabrication. It is expected that this hybrid fabrication will be extensively used in aerospace, medical, and other fields.

ACKNOWLEDGEMENTS
The authors would like to thank the financial supports from the National Natural Science Foundation of China (No. U1537105, and No. 51675273) , national key research and development plan (2018YFB1105900), and the Key Research and Development Projects of Jiangsu Province (No. BE2016010-3, No. BE2015161, and No. BE2015029). Author 1 and Author 2 contributed equally to this work.

## References

1. C.Y. Kong, R.J. Scudamore, *J. Allen, Phys. Procedia*, 5 (2010) 379.
2. C. Hong, D. Gu, D. Dai, A. Gasser, A. Weisheit, I. Kelbassa, M. Zhong, R. Poprawe, *Opt. Laser Technol.*, 54 (2013) 98.
3. O.G. Rivera, P.G. Allison, J.B. Jordon, O.L. Rodriguez, L.N. Brewer, Z. McClelland, W.R. Whittington, D. Francis, J. Su, R.L. Martens, N. Hardwick, *Mat. Sci. Eng. A-Struct*., 694 (2017) 1.
4. S. Cao, D. Gu, and Q. Shi, *J. Alloy Compd*., 692 (2017) 758.
5. G. Marchese, E. Bassini, M. Calandri, E.P. Ambrosio, F. Calignano, M. Lorusso, D. Manfredi, M. Pavese, S. Biamino, P. Fino, *Met. Powder Rep*., 71 (2016) 273.
6. C. Zhong, J. Chen, S. Linnenbrink, A. Gasser, S. Sui, R. Poprawe, *Mater. Design*, 107 (2016) 386.
7. M. Bambach, I. Sizova, F. Silze, M. Schnick, *J. Alloy Compd*., 740 (2018) 278.
8. C. Zhong, A. Gasser, J. Kittel, K. Wissenbach, R. Poprawe, *Mater. Design*, 98 (2016) 128.
9. C. Hong, D. Gu, D. Dai, M. Alkhayat, W. Urban, P. Yuan, S. Cao, A. Gasser, A. Weisheit, I. Kelbassa, M. Zhong, R. Poprawe, *Mat. Sci. Eng. A-Struct*., 635 (2015) 118.
10. M. Renderos, F. Girot, A. Lamikiz, A. Torregaray, N. Saintier, *Physics Procedia*, 83 (2016) 769.
11. X. You, Y. Tan, L. Zhao, Q. You, Y. Wang, F. Ye, J. Li, *J. Alloy Compd*., 741 (2018) 792.
12. P. Guo, X. Lin, J. Li, Y. Zhang, M. Song, W. Huang, *Corros. Sci.,* 132 (2018) 79.
13. D. Wang, Z. Zhu, N. Wang, D. Zhu, H. Wang, *Electrochim. Acta*, 156 (2015) 301.
14. X. Xu, G. Mi, L. Chen, L. Xiong, P. Jiang, X. Shao, C. Wang, *J. Alloy Compd*., 715 (2017) 362.
15. R. Andreotta, L. Ladani, W. Brindley, *Finite Elem. Anal. Des*., 135 (2017) 36.
16. T.E. Abioye, J. Folkes, A. T. Clare, *J. Mater. Process Tech*., 213 (2013) 2145.
17. Q. Shi, D. Gu, M. Xia, S. Cao, T. Rong, *Opt. Laser Technol*., 84 (2016) 9.
18. Y.L. Hu, X. Lin, X.B. Yu, J.J. Xu, M. Lei, W. D. Huang, *J. Alloy Compd.*,711 (2017) 267.
19. L.J. Kumar, C.G.K. Nair, *Mater. Today*, 4 (2017) 11068.
20. P. Guo, X. Lin, Y. Ren, J. Xu, J. Li, Y. Zhang, J. Chen, W. Huang, *Electrochim. Acta*, 276 (2018) 247.
21. T.E. Abioye, D.G. McCartney, A.T. Clare, *J. Mater. Process Tech*., 217 (2015) 232.
22. Y. Chen, F. Lu, K. Zhang, P. Nie, S.R. Elmi Hosseini, K. Feng, Z. Li, P.K. Chu, *Mater. Design,* 105 (2016) 133.
23. Z. Baicheng, L. Xiaohua, B. Jiaming, G. Junfeng, W. Pan, S. Chen-nan, N. Muiling, Q. Guojun, and W. Jun, *Mater. Design*, 116 (2017) 531.
24. C. Li, Y.B. Guo, J.B. Zhao, *J. Mater. Process Tech*., 243 (2017) 269.
25. N.S. Qu, Q.L. Zhang, X.L. Fang, E.K. Ye, D. Zhu, *Procedia CIRP,* 35 (2015) 16.
26. G. Muvvala, D. Patra Karmakar, A.K. Nath, *J. Alloy Compd.,* 740 (2018) 545.
27. X.D. Wang, N.S. Qu, P.F. Guo, X.L. Fang, X. Lin, *J. Electorchem. Soc*., 164 (2017) 548.